Ultralight and ordered lamellar polyimide-based graphene foams with efficient broadband electromagnetic absorption

Yawei Zhang[a], Shuangshuang Li[a], Xinwei Tang[a], Wei Fan[b], Qianqian Lan[a], Le Li[a], Piming Ma[a], Weifu Dong[a], Zicheng Wang[a,*], Tianxi Liu[a,*]

[a] The Key Laboratory of Synthetic and Biological Colloids, Ministry of Education, Institute of Nanocomposites and Energy Materials, School of Chemical and Material Engineering, Jiangnan University, Wuxi 214122, China
[b] State Key Laboratory for Modification of Chemical Fibers and Polymer Materials, College of Materials Science and Engineering, Donghua University, Shanghai 201620, China

A B S T R A C T

The development of high-performance microwave absorption materials with strong absorption capacity and broad bandwidth is highly desirable in the field of electromagnetic pollution protection. Herein, ultra-light polyimide-based graphene foam with ordered lamellar structure is precisely designed and control-lably constructed by bidirectional freezing process. More lamellar interfaces formed inside the foam per unit volume effectively facilitate the layer-by-layer dissipation for the vertical incident electromagnetic waves, thereby endowing the foam with efficient broadband electromagnetic absorption performance. More importantly, electromagnetic absorption performance can be controllably adjusted by optimizing impedance distribution and microstructure of skeletons. As a result, the optimized foam with an ultralow density of 9.10 mg/cm^3 presents a minimum reflection loss value of −61.29 dB at 9.25 GHz and an effective absorption bandwidth of 5.51 GHz (7.06–12.57 GHz, covering the whole X band) when the thickness is 4.75 mm.

© 2021 Published by Elsevier Ltd on behalf of Chinese Society for Metals.

1. Introduction

In order to protect electronic communication equipment and human beings from undesirable electromagnetic damage, designing and fabricating high-performance microwave absorption (MA) materials gradually becomes a significant concern in contemporary society. As a candidate to ponderous ferrites, metallic magnets, ceramics, and their hybrids, various nanomaterials, especially polymer-based porous nanocomposites, are successfully prepared and applied in the field of microwave absorption, due to the lightweight, low cost, workability, and high corrosion resistance in a harsh environment [1-4]. However, the practical application of polymer-based nanocomposites in the field of MA still faces some challenges, such as inferior absorption capacity, narrow bandwidth and single waveband.

For the polymer-based porous nanocomposites, improving the surface impedance matching can effectively promote the incident electromagnetic wave (EMW) entering the materials to the maximum extent. Furthermore, the optimization of impedance distribution and microstructure of the materials facilitates the efficient attenuation of electromagnetic waves entering the interior of the material. Therefore, a suitable impedance matching distribution and microstructure in polymer-based porous nanocomposites contributes to enhancing the dissipation of incident electromagnetic waves [5-7]. However, to date, the researches of polymer-based porous MA materials mainly focus on the random multiple reflection/scattering between the isotropic pore structures to achieve dissipation of incident electromagnetic wave [6-9]. For example, Pu et al. prepared polyimide/graphene foams with hierarchical impedance gradient structure by two-step vacuum impregnation. The sample exhibited a minimum reflection loss (RL$_{min}$) value of −32.87 dB at 10.39 GHz [6]. As reported by Zhou et al., lightweight and recoverable aramid nanofiber/reduce graphene oxide/polyimide (ANF/rGO/PI) composite aerogels were fabricated by a two-step method of freeze-drying and annealing. The aerogels exhibited an excellent RL$_{min}$ of −41.0 dB at 10.8 GHz and a broad effective absorption bandwidth (EAB, RL < −10 dB) covered the entire X-band [9]. In comparison with the isotropic random pore structure, the construction of ordered lamellar pore structure had also proved to be a method to facilitate the efficient attenuation of incident electromagnetic energy in past years [10-13]. As reported by Wang et al., highly ordered nitrogen-doped graphene

multilayer films with large interlayer void were fabricated by thermal annealing of the compact stacking graphene oxide/copper phthalocyanine multilayer films. The obtained sample revealed excellent electromagnetic interference (EMI) shielding effectiveness of 55.2 dB over the X-band [13]. However, the controllable adjustment in microstructure is restricted to thermal expansion at high temperatures. Recently, bidirectional freezing methods were employed to construct the ordered lamellar structure in composites. As reported by Gao et al., graphene aerogel was successfully prepared by a bidirectional freezing method and then carbonized at high temperatures [14]. Meanwhile, polydimethylsiloxane (PDMS) resin was encapsulated into the obtained aerogel for improving the mechanical properties. As a result, the density of the composite became larger owing to the introduction of PDMS. Additionally, Dai et al. developed a kind of polyimide/MXene aerogel by interface-reinforcement and bidirectional-freezing approach [15]. The sample exhibited a RL_{min} value of −41.8 dB. However, the large rigidity of MXene nanosheets partly hinders the formation of ordered lamellar structure in aerogels, thereby restraining the further improvement in MA performance. Therefore, how to realize the efficient construction and controllable adjustment of ultralight ordered lamellar structure by the bidirectional freezing method is still a big challenge.

In this study, we propose a facile, low-cost and effective approach to fabricate ultralight polyimide-based graphene nanocomposite foam with ordered lamellar structure by the bidirectional freezing process. As a precursor, water-soluble poly (amic acid) (PAA) can be uniformly compounded with graphene oxide (GO) in water, and transformed into polyimide after thermal imidization, thereby endowing the composite with excellent mechanical strength and thermal stability. Compared with other two-dimensional nanomaterials, the flexible graphene oxide nanosheet with a larger aspect ratio will play a more important assistant role in facilitating the formation of the ordered lamellar structure during the bidirectional freezing process. At the same time, it can be used as a pore regulating agent to adjust the lamellar spacing distance between ordered skeletons as well as freezing conditions. Meanwhile, graphene reduced from graphene oxide can be employed as a functional material for promoting the optimization of impedance matching distribution. As a consequence, the effective construction of ordered lamellar structure successfully endows polyimide/graphene foam with ultralow density, excellent MA capacity (minimum reflection loss, RL_{min}) and broad effective absorption bandwidth (EAB). More importantly, electromagnetic absorption performance also exhibits prominent adjustability by controlling impedance distribution and microstructure of skeletons at different freezing temperatures and concentration ratios of PAA and GO.

2. Experimental

2.1. Materials

Graphite powders (325 mesh) were obtained from Qingdao Jin Ri Lai Graphite Co. Ltd. (Qingdao, China). Concentrated sulfuric acid (H_2SO_4, 98%), phosphoric acid (H_3PO_4), hydrochloric acid (HCl, 37%), potassium permanganate ($KMnO_4$, ≥ 99.5%), pyromellitic dianhydride (PMDA, ≥ 98.5%), 4,4′-oxidianiline (ODA, ≥ 98.0%), triethylamine (TEA, 99%) and *N,N*-dimethylacetamide (DMAc, 99%) were purchased from Sinopharm Chemical Reagent Co., Ltd. Polydimethylsiloxane (PDMS, Sylgard 184) was purchased from Sigma-Aldrich Co., Ltd. All commercial reagents in this study were analytical grade and used without further purification.

2.2. Synthesis of graphene oxide (GO) and polyamide acid (PAA)

Graphite flakes were oxidized using the improved Hummers' method [16,17]. Water-soluble poly (amic acid) (PAA) was prepared by the condensation polymerization reaction of PMDA and ODA in an equimolar ratio using DMAc. Then, TEA was used as a hydrophilic surface modifier to prepare PAA salt. The viscous liquid was decanted into deionized water and repeatedly washed to remove the solvent and unreacted raw materials. After freeze-drying, the water-soluble PAA was obtained.

2.3. Preparation of rGO/PI foam with ordered lamellar structure

As shown in Scheme 1, GO (10 mg/mL) and PAA were uniformly mixed at the concentration ratio of 1:1. The obtained GO/PAA hydrosol was poured into a bidirectional freeze casting mould on a cold copper plate with a PDMS wedge of 15° as a spacer, which was then kept at 4 °C for 24 h for sol-gel transition. The as-prepared GO/PAA hydrogel was further frozen at −70 °C for 6 h and freeze-dried in vacuum (0.1-2 Pa, Labconco Corporation, USA). The obtained GO/PAA foam was heated to 100 °C, 200 °C and 300 °C for 1 h in nitrogen flow for the reduction of GO and imidization of PAA, which was labeled as rGO/PI-70-10c-1:1 (rGO/PI as a reference without special emphasis). For comparison, other samples of rGO/PI were also fabricated with different concentration ratios and freezing temperatures as displayed in Table 1.

2.4. Characterizations

Scanning electron microscopy (SEM) images were taken with a HITACHI S-4800 cold field-emission scanning electron microscope operated at 30 kV. X-ray diffraction (XRD) patterns were collected on a Bruker D8 X-ray diffractometer with a Cu *Kα* X-ray source (λ = 1.5418 Å). Fourier transform infrared spectroscopy (FTIR) was characterized by employing Nicolet6700 USA spectrophotometer by incorporating the samples in the KBr pellets. Thermal gravimetric analysis (TGA) was carried out by using TGA/DSC1/1100SF system under N_2 atmosphere at a heating rate of 10 °C/min. The electromagnetic parameters of the foams were measured on a vector network analyzer (Agilent 8720ET) at 0.5–18 GHz. The testing samples were fabricated by vacuum impregnating with melting paraffin and the percentage of paraffin in the samples was ∼ 85 wt%. The testing sample is cut into standard coaxial rings (outer diameter: 7.0 mm; inner diameter: 3.0 mm) along the direction perpendicular to the lamellar structure (*XZ* plane).

3. Results and discussion

3.1. Structure and morphology of composite foams

The fabrication procedure of the ordered lamellar rGO/PI composite foam was illustrated in Scheme 1. As a control, the pure poly (amic acid) (PAA) and graphene oxide (GO) were also carried out at the same bidirectional freezing conditions. However, the obtained PI and rGO foams exhibit disordered configuration as shown in Fig. 1(a) and (b), revealing an obvious difference with ordered lamellar rGO/PI foam as shown in Fig. 1(c). It may be attributed to the higher rigidity of graphene nanosheets, which heavily hinders the successive pushing of ice crystal growth during the bidirectional freezing process, leading to the formation of disordered isotropic structure in rGO foam. Therefore, the flexible PI chains become an indispensable factor and are introduced to reduce the higher rigidity of graphene foam, thereby synergistically facilitating the formation of ordered lamellar structure during the bidirectional freezing process. On the other hand, the electromagnetic insulating PI matrix is very necessary to compound with the electro-
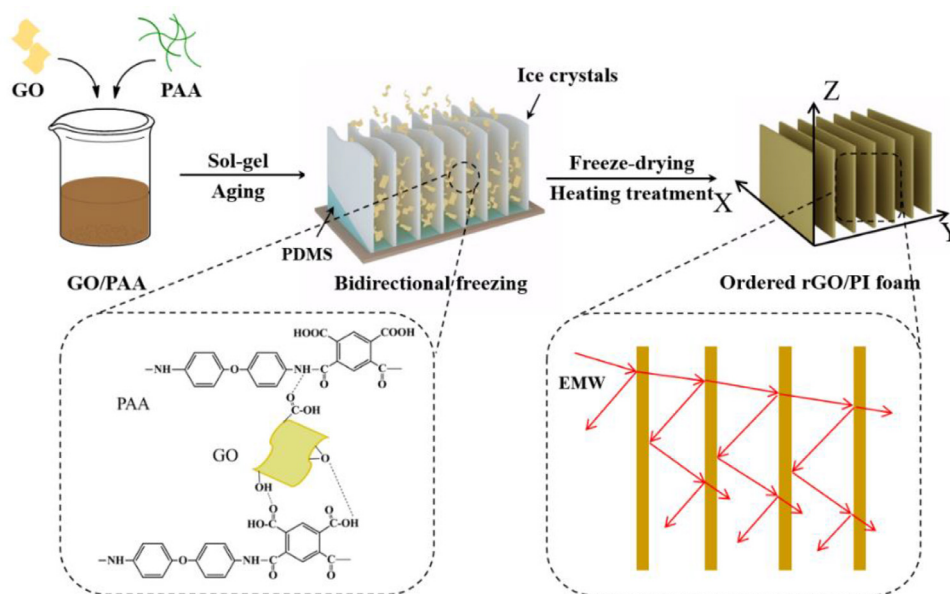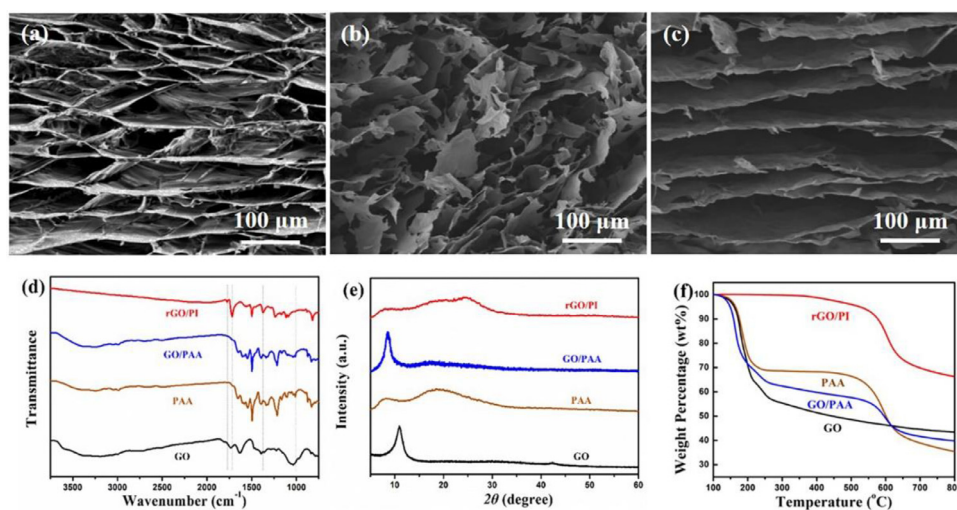
Scheme 1. The fabrication of rGO/PI foam with ordered lamellar structure.

Table 1
Sample composition of rGO/PI composite foams.

|	Freezing temperature (°C)	GO (mg/mL)	GO:PAA (mg/mL:mg/mL)
rGO/PI-50-10c-1:1	−50	10	1:1
rGO/PI-70-10c-2:1	−70	10	2:1
rGO/PI-70-10c-1:1	−70	10	1:1
rGO/PI-70-10c-1:2	−70	10	1:2
rGO/PI-70-5c-1:1	−70	5	1:1
rGO/PI-70-20c-1:1	−70	20	1:1
rGO/PI-90-10c-1:1	−90	10	1:1

Fig. 1. The cross-sectional SEM images in *XY* plane of the different foams at the same bidirectional freezing conditions: (a) PI, (b) rGO, and (c) rGO/PI; (d) FTIR, (e) XRD, and (f) TGA curves of GO, PAA, GO/PAA and rGO/PI.

magnetic functional graphene nanosheets, which makes it possible for rGO/PI to become a potential high-performance MA material.

Besides, FTIR spectra were employed to explore the chemical structure changes of PAA chains in the composite foams. As displayed in Fig. 1(d), the appearance of those characteristic absorption bands located at 3425 cm^{-1} (O–H vibrating), 1725 cm^{-1} (C=O vibrating), 1404 cm^{-1} (O–H vibrating), 1220 cm^{-1} (epoxy C–O vibrating) and 1055 cm^{-1} (alkoxy C–O vibrating) confirms the existence of oxygen functional groups on the basal plane and edge

of GO nanosheets [18]. Meanwhile, two characteristic absorption peaks arisen at 1655 cm^{-1} (C=O vibrating in -COOH and/or -CONH-) and 1604 cm^{-1} (N-H vibrating in -CONH-) can be obviously observed in the curve of PAA, which verifies the successful synthesis of PAA. After compounded with GO and thermal treatment, those peaks vanish in the rGO/PI spectrum, while new characteristic absorption peaks appear at 1775 cm^{-1} (C=O asymmetric stretching), 1716 cm^{-1} (C=O symmetrical stretching), 1371 cm^{-1} (C-N stretching in the imide ring) of the PI spectrum, respectively
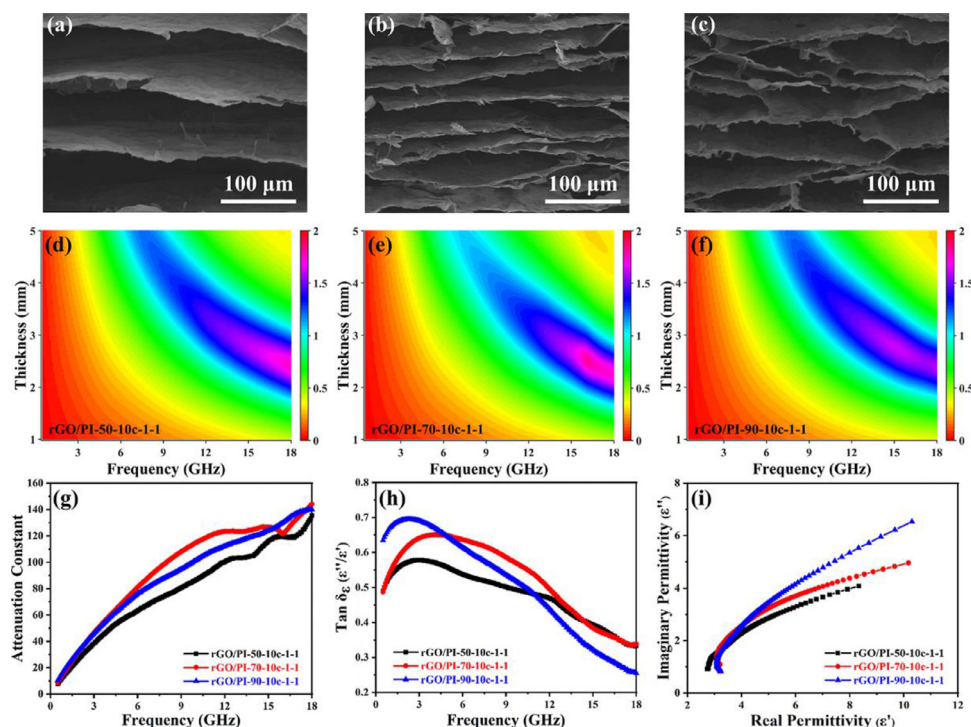
Fig. 2. The cross-sectional SEM images in the *XY* plane and 2D impedance matching contour maps ($|Z_{in}/Z_o|$) of rGO/PI foams fabricated at the freezing temperature of (a, d) −50 °C, (b, e) −70 °C, and (c, f) −90 °C; (g) attenuation constants, (h) dielectric loss tangent, and (i) Cole–Cole semicircle of the composite foams.

[19]. The above information confirms the effectiveness of the thermal treatment on the imidization of PAA chains.

The microstructure changes produced during the thermal treatment could be also identified by XRD. As depicted in Fig. 1(e), pure GO foam exhibits a sharp diffraction peak indexed to (002) centered at 10.8°, corresponding to a layer-to-layer distance of 0.83 nm. After incorporation with amorphous PAA, the stacking diffraction peak of GO/PAA foam shifts to a lower angle of 8.6° with a *d*-spacing of 1.03 nm. This 0.20 nm expansion of *d*-spacing suggests PAA chains are successfully intercalated into the GO nanosheets. After thermal treatment at 300 °C, the characteristic diffraction peak (002) of GO completely disappears, whereas a new broad peak around 24.5° arises in the curve of rGO/PI, corresponding to the (001) planes of graphene [6,13,20]. The results verify the effectiveness of the thermal treatment on the reduction of GO in GO/PAA foam.

To further probe the microstructural changes, the samples were also characterized by TGA. In comparison with GO, PAA, and GO/PAA, thermal stability of rGO/PI presents significant improvement. It can be ascribed to the decomposition of unstable functional groups in GO sheets and dehydration of PAA chains during the thermal treatment. The above result once again verifies the effectiveness of thermal treatment on the thermal reduction of GO sheets and imidization of PAA chains. As a result, it can be concluded that a kind of ordered lamellar rGO/PI foam combined with electromagnetic functional graphene sheets and high thermal stable polyimide chains has been successfully constructed, which makes it possible to become a potential high-performance MA material.

3.2. Microwave absorption properties of rGO/PI composite foams

To further investigate the effect of ordered lamellar structure on the microwave absorption properties of composite foams, the different freezing temperatures were employed to regulate the microstructure of the foams. As shown in Fig. 2(a-c), the foams fab-

ricated at the higher freezing temperature of −50 °C and −70 °C exhibit distinct ordered lamellar structures, while that of −90 °C shows a honeycomb network structure. It can be attributed to that the pushing of smaller ice crystal growth at the lower freezing temperature of −90 °C could not generate enough inner pressure to overcome the hydrogen-bonding interaction between graphene oxide sheets and PAA chains. Thus, the successive perforating pore structure in X axis direction could not be formed, which indirectly confirms the formation mechanism of ordered lamellar structure in foams. Meanwhile, it can be distinctly observed that the lamellar spacing distance of rGO/PI foams presents a tendency to increase from ∼30 to ∼100 μm with increasing the freezing temperature from −70 °C to −50 °C as depicted in Fig. 2(a) and (b). As a result, more lamellar interfaces are formed inside the foam per unit volume in −70 °C, which may contribute to the layer-by-layer dissipation for the vertical incident electromagnetic waves. Besides, as shown in Fig. S1(a) in Supporting Information, the characteristic diffraction peak of GO nanosheets shifted from 8.6° to a higher angle of 9.5° with the increasing temperature to −50 °C, implying a smaller distance between the graphene nanosheets. The increment in stacking density of skeletons leads to the fluctuation in impedance characteristic of the foam.

As a result, the competitive relationship between lamellar spacing distance and stacking density of rGO/PI skeleton synergistically endows non-magnetic rGO/PI foam with various complex permittivity ($\varepsilon_r = \varepsilon' - j\varepsilon''$) and permeability ($\mu_r = \mu' - j\mu''$, $\mu' = \sim 1.0$, $\mu'' = \sim 0.1$). As shown in Fig. S2(a, b), the samples exhibit an approximately gradual decreasing tendency in real and imagine part of permittivity with the increasing freezing temperature from −70 °C to −50 °C. The pushing of larger ice crystals at −50 °C broadens the lamellar spacing distance and hence increases the stacking density of skeletons as displayed in Figs. 1 and S1(a). The formation of the foam with a broader lamellar spacing distance allows a large amount of air included in the material, reducing the permittivity of foam. Meanwhile, the increment in stacking density of skeletons results in the improvement in the permittivity of

foam. As to rGO/PI foams, the permittivity properties are jointly determined by the lamellar spacing distance and stacking density of rGO/PI skeleton. Therefore, we can conclude that the negative impairment of increased lamellar spacing distance plays a more dominant role than the positive enhancement of increased stacking density in permittivity properties of the foams at the freezing temperature of −50 °C. In contrast, the foam fabricated at the freezing temperature of −70 °C exhibits higher permittivity properties as shown in Fig. S1. Moreover, it is worthy to note that the existence of the residuals between the lamellar spacing of the skeletons makes it possible for rGO/PI-90-10c-1-1 to form the conductive network in *X* axis direction, thereby endowing itself with a higher permittivity property.

Based on those electromagnetic parameters, the normalized characteristic impedance ($Z = |Z_{in}/Z_0|$) can be calculated by transmission line theory to evaluate the impedance matching of the composite foams according to the following Eq. (1):

$$Z_{in} = Z_0 \sqrt{\frac{\mu_r}{\varepsilon_r}} \tanh\left[j\left(\frac{2\pi f d}{c}\right)\sqrt{\mu_r \varepsilon_r}\right] \tag{1}$$

where Z_{in} and Z_0 were the impedance of composites and vacuum, respectively; μ_r was the relative permeability of the composites; ε_r was the relative permittivity of the composites; f was the frequency of microwave; d was the thickness of the composites and c was the speed of light [21-23]. As a result, the two-dimensional (2D) impedance matching contour maps of rGO/PI foams with sample thickness and measurement frequency are exhibited in Fig. 2(d-f), respectively. The color of sky blue represents the area in which Z equals 1. Therefore, achieving good impedance matching requires that the value of Z is equal or close to 1. As shown in Fig. 2(d-f), rGO/PI-70-10c-1-1 exhibits distinct optimization in impedance matching compared with other foams, meaning that more incident electromagnetic waves could enter the absorbers. It may be ascribed to the suitable stacking density pushed by ice crystal growth at −70 °C. As to the other foams, the formation of compact stacking skeletons frozen at −50 °C and the existence of the residuals between lamellar spacing frozen at −90 °C endow rGO/PI skeleton with a higher electrical conductivity, leading to the generation of surface impedance mismatching.

Meanwhile, the attenuation constant was used to quantitatively evaluate the electromagnetic energy attenuation ability of the foams, which can be calculated by Eq. (2) [24,25]: where ε' and ε'' were the real part and imaginary part of complex permittivity, and μ' and μ'' were the real part and imaginary part of complex permeability. As shown in Fig. 2(g), rGO/PI-70-10c-1-1 possesses stronger attenuation constant compared to the other samples in the high-frequency range (6–15 GHz), which is beneficial to improving electromagnetic energy attenuation. To further identify the factors contributing to the attenuation constant, the plots of ε'' vs ε' (dielectric loss tangent and Cole–Cole semicircles) for the composite foams were displayed in Fig. 2(h) and (i), respectively. For the samples, there is a distinct peak in each curve of dielectric loss tangent (Fig. 2(h)), corresponding to a Cole–Cole semicircle in Fig. 2(i). It may be caused by the interface polarization relaxation that existed between rGO nanosheet and PI chain in rGO/PI skeleton [26,27]. Moreover, it is worth noting that other loss can be confirmed by the presence of the line tail in each plot (Fig. 2(i)), which can be assigned to the conductive loss arose from the formation of conductive rGO network in rGO/PI skeletons. More importantly, as the freezing temperature decreases from −50 °C to −90 °C, the length of line tail further extends to a higher position as shown in Fig. 2(i). It implies the progressive enhancement in conductive loss [28], which is closely relative to the increasing permittivity properties of rGO/PI foams as shown in Fig. S2(a-c). However, the gradually increasing Cole–Cole semicircle presents an opposite tendency with the reduced attenuation constant with the decreasing freezing temperature from −70 °C to −90 °C. The result indirectly indicates the existence of multiple reflection/scattering loss between the internal interfaces of porous rGO/PI skeletons as demonstrated in Scheme 1. Therefore, it can be concluded that the multiple reflection/scattering loss of rGO/PI-70-10c-1-1 is higher than that of isotropous rGO/PI-90-10c-1-1, which can be attributed to the formation of ordered lamellar structures in foam, thereby propagating the dissipation path of electromagnetic wave and improving the intensity of multiple reflection/scattering loss. Therefore, the aforementioned results reveal that three main factors, including the interfacial polarization relaxation, conductive loss, and multiple reflection/scattering loss, synergistically endow rGO/PI composite foam with excellent attenuation constant.

To investigate the final microwave absorption performance, the reflection loss (RL) of the incident electromagnetic wave along the direction perpendicular to the lamellar structure (*XZ* plane) was also calculated according to Eq. (3) [29-32]:

$$RL(dB) = 20 \log \left| \frac{Z_{in} - Z_0}{Z_{in} + Z_0} \right| \tag{3}$$

As shown in Fig. 3(c, f) and Table S1, the rGO/PI-90-10c-1-1 foam possesses a RL_{min} value of −26.16 dB and a corresponding EAB value of 4.98 GHz (6.80–11.78 GHz) when the thickness and frequency are 5 mm and 8.81 GHz, respectively. After elevating the freezing temperature, the RL_{min} value of rGO/PI-70-10c-1-1 decreases to a lower value of −61.29 dB at 9.25 GHz as the thickness is set to 4.75 mm as displayed in Fig. 3(b) and (e). Meanwhile, its EAB extends to a broader value of 5.51 GHz (7.06–12.57 GHz), covering the whole X-band. The significant enhancement in absorption capacity and bandwidth can be ascribed to the successful construction of ordered lamellar structure in foam, bringing an excellent surface impedance matching and higher attenuation constant at displayed in Fig. 2. Meanwhile, rGO/PI foam exhibits obvious different MA performance along the direction paralleled to the lamellar structure (*XY* or *YZ* plane). As shown in Fig. S3, the parallel incident electromagnetic waves directly penetrate the foam without any hindrance, revealing the anisotropy of the foams for MA performance. As to rGO/PI-50-10c-1-1, the RL_{min} value of -29.18 dB is obtained when the thickness and frequency are 5.00 mm and 8.99 GHz. At this time, its EAB decreases to a narrow value of 4.99 GHz (7.06–12.05 GHz), but still covers the whole X-band. The undesired degradation of MA performance may be attributed to the worse surface impedance matching and unsatisfying attenuation constant in comparison with rGO/PI-70-10c-1-1, restraining the entry of more incident electromagnetic waves into the absorber and the efficient dissipation of EMW entering the foam interior. As a result, it once again confirms the effect of microstructure and impedance distribution on the final MA performance.

Meanwhile, based on the ordered lamellar configuration, the optimization of microstructure and impedance distribution of the composite foams will become an effective route for realizing the controllable adjustment of microwave absorption performance. As shown in Fig. 4, different concentrations of GO/PAA precursor with the same filler ratio of 1:1 are employed to fabricate the composite foams at the freezing temperature of −70 °C. It can be seen that the lamellar spacing distance between rGO/PI skeletons tends to decrease, whereas the corresponding thickness of the rGO/PI skeleton is poles apart with the increasing concentration from 5 to 20 mg/mL as shown in Fig. 4(a-c). It may be ascribed to the fact that the stronger hydrogen-bonding interaction between GO sheet and PAA chain at a higher concentration would suppress the same growth of ice crystal during the freezing process, even partly hinder the formation of ordered lamellar structure at the concentration of 20 mg/mL as depicted in Fig. 4(c). Based on impedance matching and attenuation constant, their MA performances are also calculated and displayed in Figs. S4, S5, and 4(d-f). With the
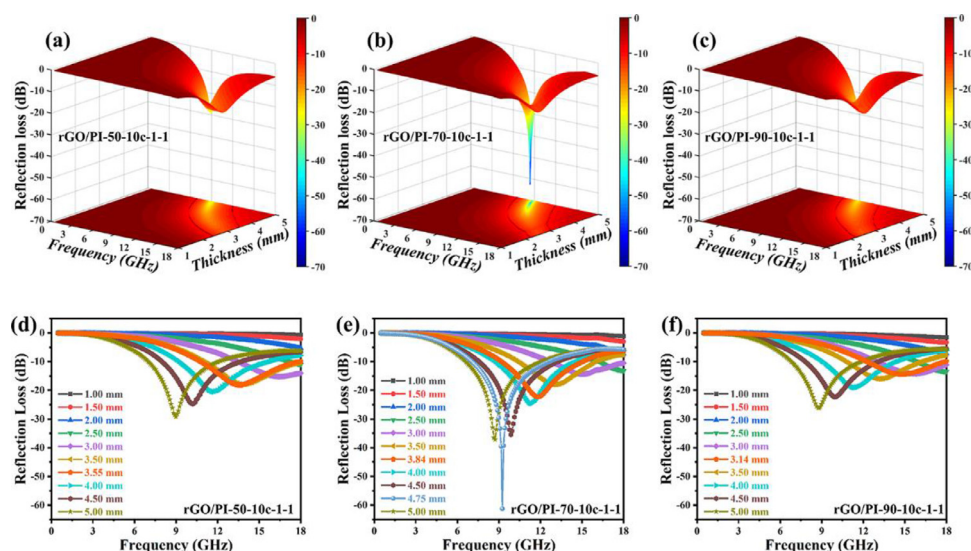
Fig. 3. 3D and 2D reflection loss maps of composite foams fabricated at different freezing temperatures: (a, d) rGO/PI-50-10c-1-1; (b, e) rGO/PI-70-10c-1-1; (c, f) rGO/PI-90-10c-1-1.
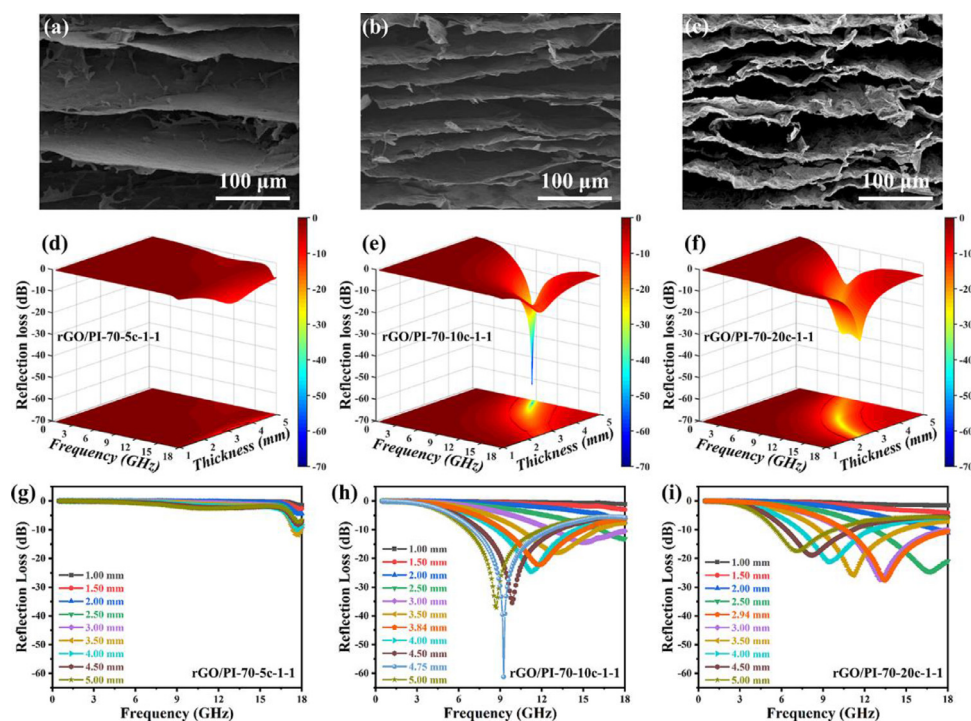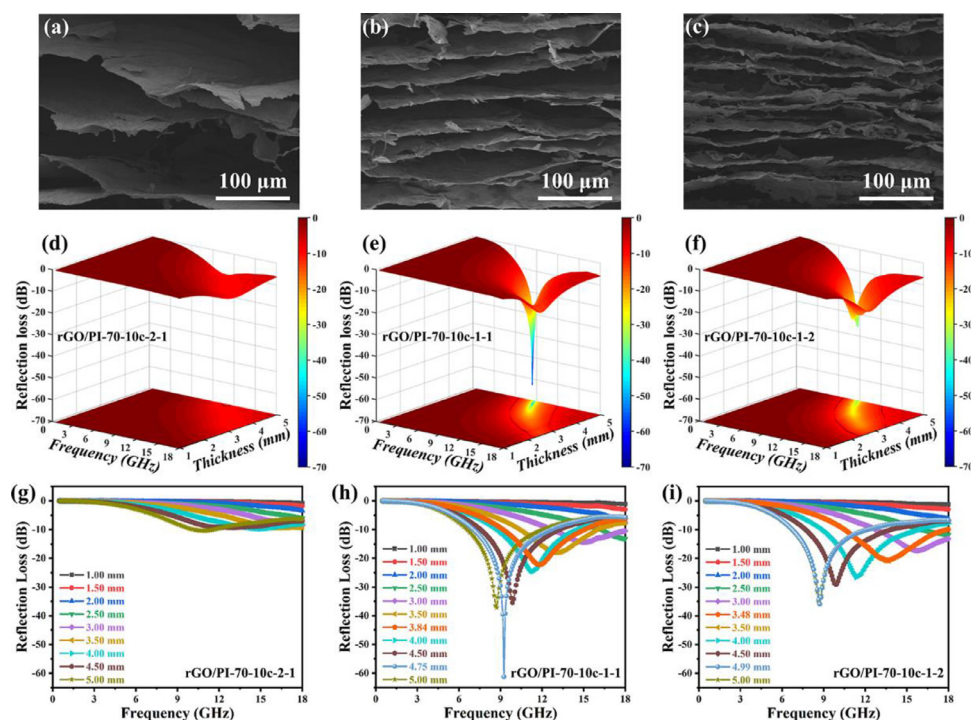

Fig. 4. The cross-sectional SEM images in the *XY* plane, 3D and 2D reflection loss maps of composite foams fabricated at different concentrations: (a, d, g) rGO/PI-70-5c-1-1; (b, e, h) rGO/PI-70-10c-1-1; (c, f, i) rGO/PI-70-20c-1-1.

increase of GO/PAA concentration, the RL_{min} value of rGO/PI shows a tendency to decrease from −11.99 dB to −61.29 dB firstly, and then increase to −28.40 dB, whereas the corresponding EAB increases from 0.61 to 5.51 GHz, and decreases to a narrow value of 3.41 GHz (Table S2), which successfully confirms the effectiveness of the microstructure and impedance distribution on controllable adjustment of MA performance.

As to rGO/PI-70-5c-1-1, the pushing of larger ice crystal growth will not only promote the formation of broader lamellar spacing between rGO/PI skeletons, but also improve the stacking density of the rGO/PI skeleton. The compact stacking of graphene sheets can be confirmed by the characteristic diffraction peak of GO shifted to a higher angle as shown in Fig. S1(b). The higher stacking density

of the rGO/PI skeleton endows it with a higher electrical conductivity, leading to the generation of surface impedance mismatching as shown in Fig. S5(a). Meanwhile, the formation of broader lamellar spacing between rGO/PI skeletons will bring a weaker attenuation constant as well as the corresponding permittivity properties as displayed in Figs. S4 and S5, which agrees with the results of rGO/PI frozen at -50°C. As a consequence, the rGO/PI-70-5c-1-1 foam exhibits an inferior MA capacity and bandwidth as shown in Fig. 4(g).

As a control, with the increasing concentration of rGO/PI, the gradually enhanced hydrogen-bonding interaction hinders the ice crystal growth during freezing process, thereby inducing the more lamellar interfaces formed inside the foam per unit volume as

Fig. 5. The cross-sectional SEM images in *XY* plane, 3D and 2D reflection loss maps of composite foams fabricated at different filler ratios: (a, d, g) rGO/PI-70-10c-2-1; (b, e, h) rGO/PI-70-10c-1-1; (c, f, i) rGO/PI-70-10c-1-2.

shown in Fig. 4(b) and (c). As a result, the surface impedance matching and attenuation constant derived from surface polarization loss, conductive loss and multiple reflection loss can be further optimized. As shown in Fig. S5, the attenuation constant of rGO/PI-70-20c-1-1 is higher than that of rGO/PI-70-10c-1-1, whereas the surface impedance matching of them shows a reverse improvement. It may be due to the complex competition relationship between pushing of ice crystal growth and hindrance of hydrogen-bonding interaction at high concentration. Under the synergistic effect of optimized impedance matching and attenuation characteristics, the foams exhibit obvious differences in MA performance as shown in Fig. 4(h) and (i). More importantly, based on the final MA performance, we can also conclude that a good impedance matching will play a more crucial role than attenuation constant in facilitating the entry of more incident electromagnetic wave into the foams, thereby allowing the effective dissipation of incident EMWs as much as possible.

Besides, the influence of filler ratios between graphene sheets and PI chains in rGO/PI skeleton on the final MA performance is further investigated and displayed in Fig. 5. As shown in Fig. 5(a), the presence of rigid graphene nanosheets at a higher filler ratio of 2:1 still hinders the formation of ordered lamellar structure, leading to the generation of incompact disordered structure in foam. The higher filler ratio of conductive graphene combined with fluffy microstructure endows rGO/PI-70-10c-2-1 with an undesirable surface impedance matching and inferior attenuation constant as shown in Figs. S6 and S7. Hence, an embarrassed MA performance with a RL_{min} value of −10.38 dB and EAB of 1.40 GHz is inevitably obtained at a higher frequency of 11.0 GHz when the thickness is controlled at 5.00 mm (Fig. 5(g) and Table S3). As the filler ratio of PI increases, the introduction of thermoplastic flexible PI chains can effectively promote the controllable construction of ordered lamellar structures in foams, and more lamellar interfaces can be formed inside the foam per unit volume as shown in Fig. 5(b) and (c). The results once again confirm the effectiveness of filler ratio on controllable adjustment of microstructure in

foams. As a consequence, the further optimized surface impedance matching and enhanced attenuation constant jointly facilitate the improvement in the final MA performance as shown in Fig. 5(h), 5(i), S6, and S7. It is worthy to note that EAB of rGO/PI-70-10c-1-2 can remain a comparable value of 5.25 GHz, although the RL_{min} value increases to −35.91 dB. More importantly, the maximum of effective absorption bandwidth (EAB_{max}) can reach a broader value of 7.44 GHz (10.56-18 GHz), covering the mid-high frequency band. It may be ascribed to the formation of more lamellar interfaces formed inside the foam per unit volume, inducing a stronger multiple reflection/scattering loss, surface polarization loss, and conductive loss as displayed in Fig. S7(b-f).

For comparison, Table 2 lists the recently reported porous materials and their corresponding MA performance [6, 8, 33-40]. As summarized in Table 2, the rGO/PI foam with ordered lamellar structures exhibits a distinct competitive advantage in contrast to other porous materials. For example, MXene/cellulose aerogel with a density of 310 mg/cm^3 presented a RL_{min} value of −43.4 dB and EAB of 4.5 GHz [34]. Jiang et al. prepared a spongy bone-like graphene@SiC (TGO@SiC) aerogel with a density of 72 mg/cm^3 [37]. The RL_{min} value reached −47.3 dB and the corresponding EAB was up to 4.7 GHz. In this study, the rGO/PI-70-10c-1-1 with an ultralow density of 9.10 mg/cm^3 shows a more excellent RL_{min} value of −61.29 dB and a broader EAB of 5.51 GHz. Meanwhile, similar phenomena can be observed for Graphene/TPU foam and GPFA [35,36,38-40]. Therefore, we can conclude that the excellent broadband microwave absorption performance combined with ultralow density makes it possible for rGO/PI foam to become an efficient microwave attenuation material with a great potential to be deployed in aerospace and aviation fields.

4. Conclusion

In summary, ultralight polyimide-based graphene foam with ordered lamellar structure is precisely designed and controllably constructed by bidirectional freezing process. The more lamellar inter-

Table 2

Microwave absorption properties of carbon-based composite foams reported recently.

	Density (mg/cm^3)	Thickness (mm)	RL$_{min}$ (dB)	EAB (GHz)	Range (GHz)	Ref.
MXene/PI	8.9	3.0	−45.4	3.7	8.3–12.0	[33]
MXene/cellulose	310	2.0	−43.4	4.5	9.6–14.1	[34]
Graphene/TPU foam	310	1.6	−32.0	4.7	/	[35]
GPFA	38.3	3.0	−49.2	6.1	9.8–15.9	[36]
Graphene aerogel	4.76	5.0	−14.0	3.73	8.16–11.89	[8]
PI-GP$_{1/3}$-rGO	63.7	4.0	−32.9	6.22	8.26–14.48	[6]
TGO@SiC	72	3	−47.3	4.7	8.5–13.2	[37]
GPEGs	19.8	2.35	−43.2	5.3	9.6–14.9	[38]
FeNi@NC/NCNT/N-rGO	13.1	2	−39.39	4.7	/	[39]
SiCnw@SiC foam	125	2.82	−52.49	5.6	9.6–15.2	[40]
rGO/PI-70-10c-1-1	9.10	4.75	−61.29	5.51	9.25–15.11	This Work

faces formed inside the foam per unit volume effectively facilitate the layer-by-layer dissipation for the vertical incident electromagnetic waves, thereby endowing the foam with efficient broadband electromagnetic absorption performance. Meanwhile, electromagnetic absorption performance can be controllably adjusted by optimizing impedance distribution and microstructure of rGO/PI skeletons at different freezing temperatures and concentration ratios of PAA and GO. As a result, the optimized rGO/PI foam with an ultralow density of 9.10 mg/cm^3 exhibits an excellent RL$_{min}$ value of -61.29 dB at 9.25 GHz and a broad EAB of 5.51 GHz (7.06–12.57 GHz), covering the whole X-band, which makes it promising to be an efficient electromagnetic absorption material with a distinct competitive advantage.

Acknowledgments

Supplementary materials

Supplementary material associated with this article can be found, in the online version, at doi:10.1016/j.jmst.2021.07.011.

References

[1] L. Wang, Z.L. Ma, L.X. Chen, Y.L. Zhang, D.P. Cao, J.W. Gu, SusMat (2021), doi:10.1002/sus2.21.
[2] H. Chen, B. Zhao, Z.F. Zhao, H.F. Xiang, F.Z. Dai, J.C. Liu, Y.C. Zhou, J. Mater. Sci. Technol. 47 (2020) 216–222.
[3] X.T. Yang, S.G. Fan, Y. Li, Y.Q. Guo, K.P. Ruan, Y.G. Li, S.M. Zhang, J.L. Zhang, J. Kong, J.W. Gu, Compos., Part A 128 (2020) 105670.
[4] C. Chen, S.F. Zeng, X.C. Han, Y.Q. Tan, W.L. Feng, H.H. Shen, S.M. Peng, H.B. Zhang, J. Mater. Sci. Technol. 54 (2020) 223–229.
[5] P. Song, B. Liu, H. Qiu, X.T. Shi, D.P. Cao, J.W. Gu, Compos. Commun. 24 (2021) 100653.
[6] L. Pu, S.S. Li, Y.W. Zhang, H.Y. Zhu, W. Fan, P.M. Ma, W.F. Dong, Z.C. Wang, T.X. Liu, J. Mater. Chem. C 9 (2021) 2086–2094.
[7] P. Song, B. Liu, C.B. Liang, K.P. Ruan, H. Qiu, Z.L. Ma, Y.Q. Guo, J.W. Gu, Nano-Micro Lett. 13 (2021) 91.
[8] Z.C. Wang, R.B. Wei, J.W. Gu, H. Liu, C.T. Liu, C.J. Luo, J. Kong, Q. Shao, N. Wang, Z.H. Guo, X.B. Liu, Carbon 139 (2018) 1126–1135.
[9] Y. Zhou, S.J. Wang, D.S. Li, L. Jiang, Compos., Part B 213 (2021) 108701.
[10] X. Zhang, X.Y. Zhao, T.T. Xue, F. Yang, W. Fan, T.X. Liu, Chem. Eng. J. 385 (2020) 123963.
[11] W.L. Song, M.S. Cao, L.Z. Fan, M.M. Lu, Y. Li, C.Y. Wang, H.F. Ju, Carbon 77 (2014) 130–142.
[12] W.L. Song, L.Z. Fan, M.S. Cao, M.M. Lu, C.Y. Wang, J. Wang, T.T. Chen, Y. Li, Z.L. Hou, J. Liu, Y.P. Sun, J. Mater. Chem. C 2 (2014) 5057–5064.
[13] Z.C. Wang, R.B. Wei, X.B. Liu, ACS Appl. Mater. Interfaces 9 (2017) 22408–22419.
[14] W.W. Gao, N.F. Zhao, T. Yu, J.B. Xi, A.R. Mao, M.Q. Yuan, H. Bai, C. Gao, Carbon 157 (2020) 570–577.
[15] Y. Dai, X.Y. Wu, Z.S. Liu, H.B. Zhang, Z.Z. Yu, Compos., Part B 200 (2020) 108263.
[16] K.P. Ruan, Y.Q. Guo, Y.S. Tang, Y.L. Zhang, J.N. Zhang, M.K. He, J. Kong, J.W. Gu, Compos. Commun. 10 (2018) 68–72.
[17] C. Daniela, D.V.K. Marcano, J.M. Berlin, A. Sinitskii, Z.Z. Sun, A. Slesarev, L.B. Alemany, W. Lu, J.M. Tour, ACS Nano 4 (2010) 4806–4814.
[18] K.P. Ruan, Y.Q. Guo, C.Y. Lu, X.T. Shi, T.B. Ma, Y.L. Zhang, J. Kong, J.W. Gu, Research 2021 (2021) 8438614.
[19] J. Li, G.C. Song, J.R. Yu, Y. Wang, J. Zhu, Z.M. Hu, Nanomaterials 7 (2017) 395.
[20] L. Wang, X.T. Shi, J.L. Zhang, Y.L. Zhang, J.W. Gu, J. Mater. Sci. Technol. 52 (2020) 119–126.
[21] B.W. Deng, Z. Xiang, J. Xiong, Z.C. Liu, L.Z. Yu, W. Lu, Nano-Micro Lett. 12 (2020) 55.
[22] Z.Y. Jiang, H.X. Si, X. Chen, H.M. Liu, L. Zhang, Y.H. Zhang, C.H. Gong, J.W. Gu, Compos. Commun. 22 (2020) 100503.
[23] R.W. Shu, G.Y. Zhang, C. Zhang, Y. Wu, J.B. Zhang, Adv. Electron. Mater. 7 (2021) 2001001.
[24] R.W. Shu, Z.L. Wan, J.B. Zhang, Y. Wu, Y. Liu, J.J. Shi, M.D. Zheng, ACS Appl. Mater. Interfaces 12 (2020) 4689–4698.
[25] S. Dong, P.T. Hu, X.T. Li, C.Q. Hong, X.H. Zhang, J.C. Han, Chem. Eng. J. 398 (2020) 125588.
[26] R.W. Shu, J.B. Zhang, Y. Wu, Z.L. Wan, X.H. Li, Nanoscale 13 (2021) 4485–4495.
[27] C.X. Wang, B.B. Wang, X. Cao, J.W. Zhao, L. Chen, L.G. Shan, H.N. Wang, G.L. Wu, Compos., Part B 205 (2021) 108529.
[28] X.N. Chen, Y. Zhang, L. Tao, Q.Q. Nie, F.C. Meng, S.B. Zhu, L.Y. Cui, R.X. Huang, Carbon 164 (2020) 224–234.
[29] B. Zhao, J.S. Deng, C.X. Zhao, C.D. Wang, Y.G. Chen, M. Hamidinejad, R.S. Li, C.B. Park, J. Mater. Chem. C 8 (2020) 58–70.
[30] J.S. Hua, W.J. Ma, X.Y. Liu, Q.X. Zhuang, Z.Y. Wu, H. Huang, S.L. Lin, J. Mater. Chem. C 8 (2020) 16489–16497.
[31] T.T. Bai, Y. Guo, D.D. Wang, H. Liu, G. Song, Y.M. Wang, Z.H. Guo, C.T. Liu, C.Y. Shen, J. Mater. Chem. A 9 (2021) 5566–5577.
[32] J. Zhao, J.L. Zhang, L. Wang, J.K. Li, T. Feng, J.C. Fan, L.X. Chen, J.W. Gu, Compos. Commun. 22 (2020) 100486.
[33] J. Liu, H.B. Zhang, X. Xie, R. Yang, Z.S. Liu, Y.F. Liu, Z.Z. Yu, Small 14 (2018) 1802479.
[34] Y. Jiang, X. Xie, Y. Chen, Y. Liu, R. Yang, G. Sui, J. Mater. Chem. C 6 (2018) 8679–8687.
[35] Y. Gao, C. Wang, J. Li, S. Guo, Compos., Part A 117 (2019) 65–75.
[36] C. Zhang, Y. Chen, H. Li, R. Tian, H. Liu, ACS Omega 3 (2018) 5735–5743.
[37] Y. Jiang, Y. Chen, Y.J. Liu, G.X. Sui, Chem. Eng. J. 337 (2018) 522–531.
[38] H.M. Ji, J.H. Li, J.J. Zhang, Y. Yan, Compos., Part A 123 (2019) 158–169.
[39] J. Xu, X. Zhang, H.R. Yuan, S. Zhang, C.L. Zhu, X.T. Zhang, Y.J. Chen, Carbon 159 (2020) 357–365.
[40] K. Su, Y. Wang, K.X. Hu, X. Fang, J. Yao, Q. Li, J. Yang, ACS Appl. Mater. Interfaces 13 (2021) 22017–22030.